

## RESEARCH ARTICLE

10.1002/2016JA023517

## Special Section:

Major Results From the MAVEN Mission to Mars

## Key Points:

- The total  $>6$  eV  $O^+$  ion escape rate increases from  $2$  to  $3 \times 10^{24} s^{-1}$  as the EUV irradiance increases by almost the same factor
- The tailward escape rate increases with EUV, while the plume escape rate does not change significantly
- The ratio of the plume escape to the total escape drops from  $\sim 30\%$  to  $\sim 20\%$  as the EUV increases

## Correspondence to:

Y. Dong,  
yaxue.dong@lasp.colorado.edu

## Citation:

Dong, Y., X. Fang, D. A. Brain, J. P. McFadden, J. S. Halekas, J. E. P. Connerney, F. Eparvier, L. Andersson, D. Mitchell, and B. M. Jakosky (2017), Seasonal variability of Martian ion escape through the plume and tail from MAVEN observations, *J. Geophys. Res. Space Physics*, 122, doi:10.1002/2016JA023517.

Received 25 SEP 2016

Accepted 23 FEB 2017

## Seasonal variability of Martian ion escape through the plume and tail from MAVEN observations

Y. Dong<sup>1</sup> , X. Fang<sup>1</sup> , D. A. Brain<sup>1</sup> , J. P. McFadden<sup>2</sup>, J. S. Halekas<sup>3</sup> , J. E. P. Connerney<sup>4</sup> , F. Eparvier<sup>1</sup> , L. Andersson<sup>1</sup> , D. Mitchell<sup>2</sup> , and B. M. Jakosky<sup>1</sup> <sup>1</sup>Laboratory for Atmospheric and Space Physics, University of Colorado Boulder, Boulder, Colorado, USA, <sup>2</sup>Space Science Laboratory, University of California, Berkeley, California, USA, <sup>3</sup>Department of Physics and Astronomy, University of Iowa, Iowa City, Iowa, USA, <sup>4</sup>Goddard Space Flight Center, NASA, Greenbelt, Maryland, USA

**Abstract** We study the Mars Atmosphere and Volatile Evolution spacecraft observations of Martian planetary ion escape during two time periods: 11 November 2014 to 19 March 2015 and 4 June 2015 to 24 October 2015, with the focus on understanding the seasonal variability of Martian ion escape in response to the solar extreme ultraviolet (EUV) flux. We organize the  $>6$  eV  $O^+$  ion data by the upstream electric field direction to estimate the escape rates through the plume and tail. To investigate the ion escape dependence on the solar EUV flux, we constrain the solar wind dynamic pressure and interplanetary magnetic field strength and compare the ion escape rates through the plume and tail in different energy ranges under high and low EUV conditions. We found that the total  $>6$  eV  $O^+$  escape rate increases from  $2$  to  $3 \times 10^{24} s^{-1}$  as the EUV irradiance increases by almost the same factor, mostly on the  $<1$  keV tailward escape. The plume escape rate does not vary significantly with EUV. The relative contribution from the plume to the total escape varies between  $\sim 30\%$  and  $\sim 20\%$  from low to high EUV. Our results suggest that the Martian ion escape is sensitive to the seasonal EUV variation, and the contribution from plume escape becomes more important under low EUV conditions.

## 1. Introduction

The neutral gas in the Martian atmosphere can be ionized by the solar extreme ultraviolet (EUV) radiation, solar wind electron impact, and charge-exchange collisions with ions. These processes produce planetary ions including mainly  $O^+$ ,  $O_2^+$ , and  $CO_2^+$ . The solar wind plasma and moving interplanetary magnetic field (IMF) generate a convection electric field ( $\mathbf{E} = -\mathbf{U} \times \mathbf{B}$ ) at Mars. Without the shielding from an intrinsic global magnetic field, the newly produced planetary ions can be stripped away by the solar wind and IMF through the pickup process. The gyroradii of these pickup ions are very large in the solar wind and sheath region, usually on a scale of a few Mars radii. As shown in many numerical models [Cloutier *et al.*, 1974; Luhmann and Schwingenschuh, 1990; Brecht and Ledvina, 2006; Fang *et al.*, 2008; Najib *et al.*, 2011; Dong *et al.*, 2014; Jarvinen *et al.*, 2015; Curry *et al.*, 2015], a portion of pickup ions generated are accelerated by the strong electric field in the sheath region and solar wind for a long distance before finally being deflected to the solar wind direction, forming a plume-like structure of energetic escaping ions mainly in the upstream electric field direction. The pickup ions generated close to the planet are affected more by the strong magnetic field. They will eventually drift to the solar wind direction and escape through the tail region.

Ion escape at Mars has been observed by the Phobos and Mars Express (MEX) spacecraft [Lundin *et al.*, 1989, 2004]. Barabash *et al.* [2007] estimated that the total heavy ion escape rate at  $>30$  eV was  $\sim 4 \times 10^{23} s^{-1}$  based on MEX data from 2004 to 2006. The escape rates including lower energy ions estimated using Phobos and MEX data at different times vary by an order of magnitude from  $2 \times 10^{24} s^{-1}$  to  $3 \times 10^{25} s^{-1}$  [Lundin *et al.*, 1990, 2008a; Fränzl *et al.*, 2010; Nilsson *et al.*, 2011; Ramstad *et al.*, 2013]. Ion escape at Mars can be affected by a number of factors, such as solar wind, IMF, solar radiation, and the crustal magnetic field. There have been studies of the Martian ion escape variation based on different energy ranges and time periods. Lundin *et al.* [2008b] studied the low-energy (30–800 eV) ion data from MEX during 17 months from 2004 to 2006 and found positive correlations of the low-energy ion escape with both solar wind dynamic pressure and EUV flux. Another study by Nilsson *et al.* [2010] using 1.5 year MEX data from 2004 to 2005 within a larger energy range of 30 eV–36 keV showed that the escaping ion fluxes increase with the subsolar magnetic field strength but found no clear correlation between the ion escape and solar EUV. Lundin *et al.*'s [2013] study of  $<300$  eV ion escape based on MEX data during a much longer time period (2007–2013) shows a strong

dependence of the ion escape with solar activity measured by the  $F_{10.7}$  index and sunspot numbers. More recently, *Ramstad et al.* [2015] also performed a statistical study using 7 year (2007–2014) MEX data in a bigger energy range of 10 eV – 15 keV to investigate the relationship between the ion escape rate and the solar wind density and velocity under high and low EUV conditions. It is worth noting that these work based on Phobos and MEX data focused on the tailward ion escape. Although energetic ion beams with similar characteristics to the plume ions were detected sporadically [*Kallio et al.*, 1995; *Carlsson et al.*, 2006, 2008; *Dubin et al.*, 2006; 2011], a substantial plume feature was not established by Phobos or MEX observations, most likely due to the lack of IMF measurements and limited instrument field of view (FOV) [*Liemohn et al.*, 2014]. Thus, these previous ion escape rates may be underestimated. The plume contribution to the total ion escape and its variability with upstream conditions were not clear yet.

The Mars Atmosphere and Volatile Evolution (MAVEN) spacecraft [*Jakosky et al.*, 2015] arrived at Mars in September 2014. Equipped with instruments to measure plasma, magnetic field, and solar EUV radiation, MAVEN has provided unprecedented opportunity to study ion escape at Mars in the context of solar wind, IMF, and solar radiation conditions. Based on the MAVEN data from November 2014 to March 2015 near solar maximum, the total escape rate for all heavy ion species at  $>25$  eV is estimated to be  $\sim 3 \times 10^{24} \text{ s}^{-1}$  through a spherical surface around Mars [*Brain et al.*, 2015], almost 1 order of magnitude higher than the previous MEX result with a very similar energy threshold ( $>30$  eV) estimated near solar minimum [*Barabash et al.*, 2007], which indicates a drastic long-term time variability of Martian ion escape over the past decade. Using MAVEN planetary ion data organized by the upstream electric field direction, we confirmed the existence of a substantial plume of energetic escaping ions mainly in the electric field direction generally consistent with model predictions, which contributes 23% of the total escape rate for  $>25$  eV  $\text{O}^+$  ions [*Dong et al.*, 2015]. In this paper we will reanalyze the first 4 months of MAVEN data with a lower energy threshold of 6 eV enabled by updated data calibrations and also include additional MAVEN data during a later time period in 2015, when the solar EUV flux is significantly different. Although there have been studies of the Martian ion escape variation with solar EUV based on MEX data [*Lundin et al.*, 2008b, 2013; *Nilsson et al.*, 2010; *Ramstad et al.*, 2015], the effects from solar wind and/or IMF are not excluded and the variation of the plume escape has never been investigated. With MAVEN data, we will be able to constrain both solar wind and IMF conditions to investigate the seasonal variations of ion escape through the two different channels (plume and tail) in response to solar EUV.

## 2. MAVEN Instruments and Data

This work is based on the planetary ion data from the Suprathermal and Thermal Ion Composition (STATIC) instrument [*McFadden et al.*, 2015]. STATIC consists of an electrostatic analyzer that detects positive ions in an energy-to-charge range of 0.1 eV/e to 30 keV/e within a FOV of  $360^\circ \times 90^\circ$  and a time-of-flight mass spectrometer that can resolve the major ion species ( $\text{H}^+$ ,  $\text{He}^{++}$ ,  $\text{O}^+$ ,  $\text{O}_2^+$ ,  $\text{CO}_2^+$ , etc.) near Mars. We use the “d0” data product from STATIC, which has 32 energy bins, 8 mass bins,  $32 \times 4$  angular bins, and a time resolution of  $\leq 128$  s. Although STATIC has a limited FOV, its orientation can change several times during one spacecraft orbit to better detect ion fluxes from different directions.

The upstream solar wind and IMF are measured by the Solar Wind Ion Analyzer (SWIA) [*Halekas et al.*, 2015] and Magnetometer (MAG) [*Connerney et al.*, 2015]. The MAVEN EUV Monitor (EUVM) has three channels: Channel A 17–22 nm, Channel B 0.1–7 nm, and Channel C 121–122 nm [*Eparvier et al.*, 2015]. In this study we use the data from Channel A to represent the solar EUV radiation.

Depending on different locations near Mars, the spacecraft potential can be estimated from STATIC, the Solar Wind Electron Analyzer instrument [*Mitchell et al.*, 2016], and/or the Langmuir Probe and Waves instrument [*Andersson et al.*, 2015] data. Combining these spacecraft potential corrections from different instruments, we are able to extend the lower energy limit to 6 eV for planetary data analysis.

## 3. MAVEN Observations of Ion Escape During Two Time Periods

We examine MAVEN data from two time periods: 11 November 2014 to March 19 2015 (Time 1) and 4 June 2015 to 24 October 2015 (Time 2). These two time intervals represent different Mars seasons: the planet was passing perihelion during Time 1 and was approaching aphelion during Time 2. The spacecraft orbits in the

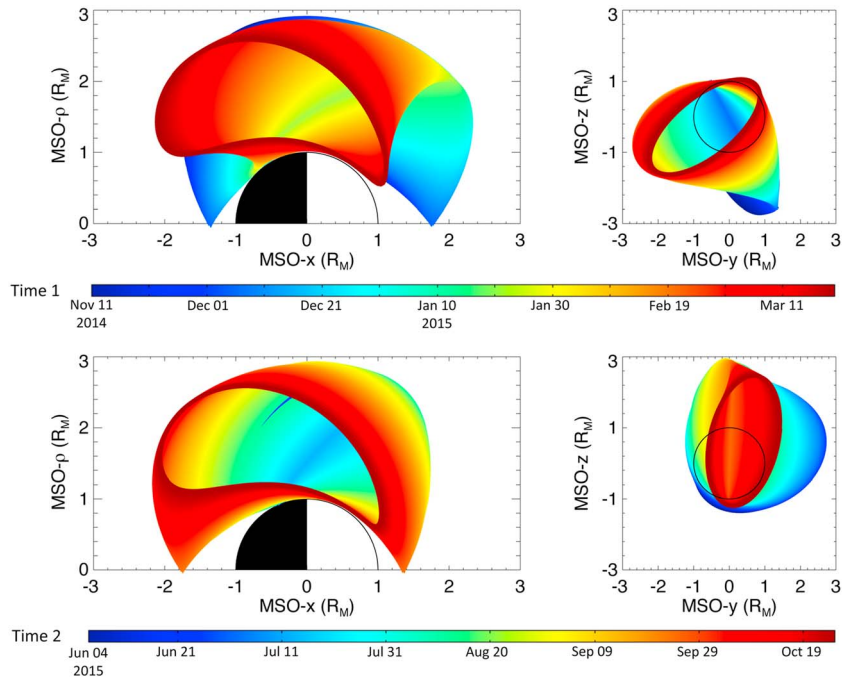


**Figure 1.** MAVEN orbits in the MSO coordinate system during two time periods, where  $\rho = \sqrt{y^2 + z^2}$ . The y-z planes in the right column are viewed from the +x direction.

Mars-Sun-Orbit (MSO) coordinate system (x axis pointing toward the Sun, z axis parallel to the normal of Mars orbital plane, and y axis completing the right-hand system) are shown in Figure 1. During these two time periods, MAVEN crossed the bow shock during most of the orbits and had direct solar wind and IMF measurements. Using the orbit-averaged IMF data [Halekas et al., 2016] from MAG, we can organize the planetary ion data from STATIC in the Mars-Solar-Electric field (MSE) coordinate system, with x axis pointing to the Sun, z axis in the upstream electric field direction, and y axis completing the right-hand system.

Figures 2a–2f show the mean number fluxes and velocities for  $>6$  eV  $O^+$  ions projected to the MSE x-z plane. The values in each  $(0.2 R_M)^2$  bin have been averaged over the y direction. These maps from the two different time periods show a consistent ion flow pattern near Mars: energetic plume fluxes in the +E (+z) hemisphere, slower tailward fluxes on the nightside, and weak precipitating ion fluxes [Hara et al., 2013; Leblanc et al., 2015] on the dayside of the –E hemisphere. We can also see some differences between the two time periods: stronger tailward fluxes and higher plume velocities during Time 1 than those during Time 2.

Figures 2g–2l show the escaping ion fluxes through the plume and tail cross sections at  $z=1.6 R_M$  and  $x=-1.6 R_M$  as marked in Figures 2a–2c, which are integrated to obtain the plume and tail escape rates. These surfaces are chosen for decent data coverage and reasonable distance from the planet. The ion fluxes in Figures 2g–2l are averaged within  $0.2 R_M$  below and above the surfaces. As discussed [Dong et al., 2015], the STATIC instrument limited FOV can affect the estimation of ion fluxes. Thus, when calculating the plume (tailward) escape rate, we only use the data points when the MSE +z (–x) direction is within the STATIC FOV to ensure that the major portion of the ion fluxes is reasonably captured. Only these data points are used to calculate the fluxes in Figures 2g–2l.

We apply two different methods to calculate the ion escape rates. The first method is to integrate only over the data covered areas at  $x > -1.6 R_M$  for the plume cross sections and at  $z < 1.6 R_M$  for the tail cross sections. The cuts at  $x = -1.6 R_M$  and  $z = 1.6 R_M$  are meant to avoid double counting the escaping ions. The data covered areas and escape rates are shown in Table 1 (numbers in the parentheses). These estimates are the lower limits of the escape rates, because the data points do not cover the full surfaces. As shown in Table 1, the data covered areas in the parentheses are different for the same surface between the two time periods, which will cause bias for the escape rate comparisons. Thus, we also apply a second method: to define an integration area for the plume and tail cross sections as shown by the dashed lines in

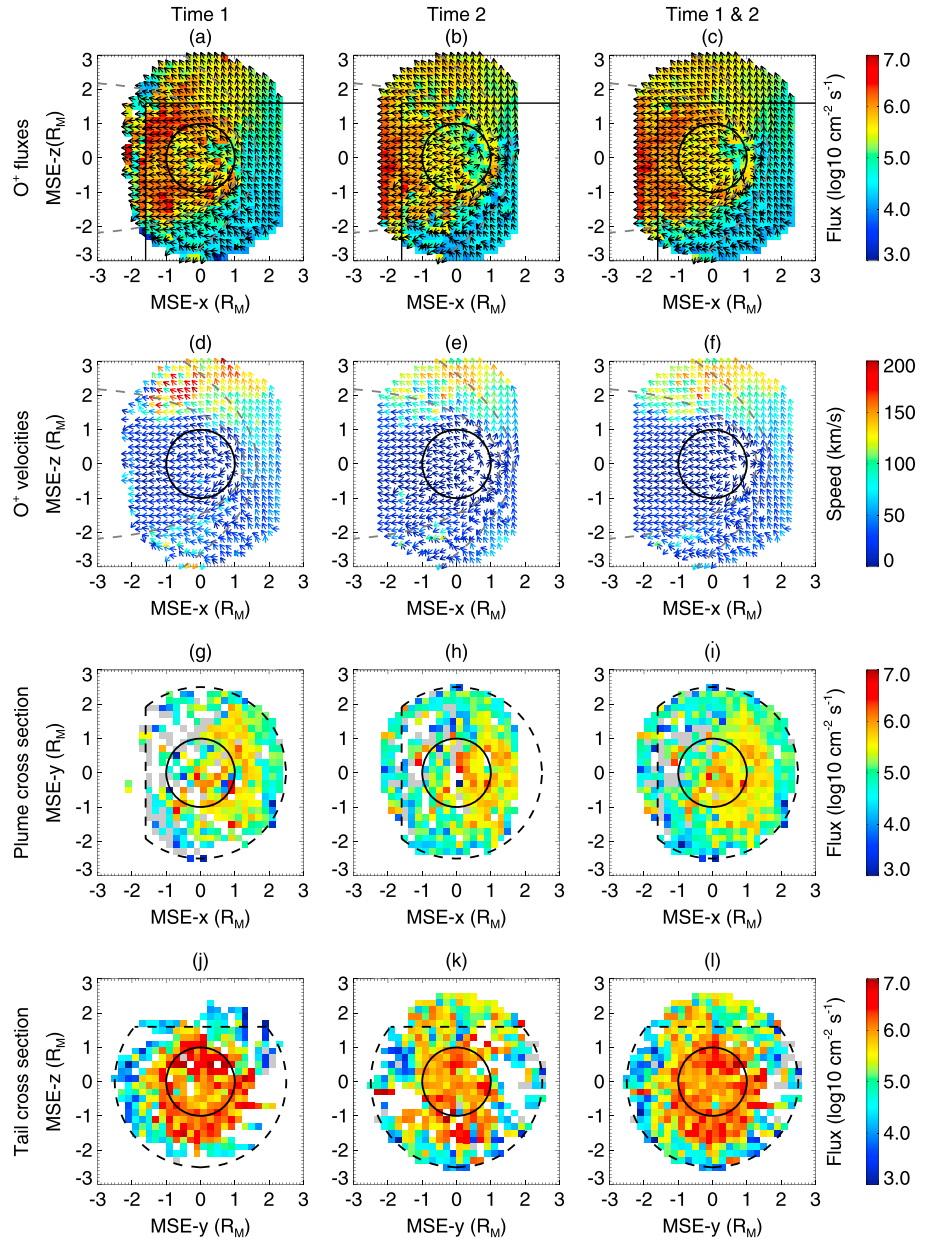


**Figure 2.** (a–f)  $O^+$  ion flux and velocity maps in the MSE  $x$ - $z$  plane, averaged over the  $y$  axis and viewed from the  $+y$  direction. The grey dashed lines are the model bow shock and MPB from *Vignes et al.* [2000]. (g–l) The escaping ion fluxes through the plume and tail cross sections at  $z = 1.6 R_M$  and  $x = -1.6 R_M$  as shown by the black solid lines in Figures 2a–2c. The black dashed lines label the areas used for ion escape rate calculations. The grey bins represent returning fluxes. The viewing directions for the plume and tail cross sections are the  $+z$  and  $+x$  directions, respectively.

Figures 2g–2l. The integration area is defined as  $x > -1.6 R_M$  and  $\sqrt{x^2 + y^2} \leq 2.5 R_M$  for the plume cross section and  $z < 1.6 R_M$  and  $\sqrt{y^2 + z^2} \leq 2.5 R_M$  for the tail cross section. We calculate the mean fluxes within these areas and then use these mean fluxes and areas to calculate the escape rates. In this way the escape rates are estimated over the same integration areas, which avoids the bias from different data covered areas between the two time periods. The radial limit  $2.5 R_M$  is chosen because the data points covered the major portion of the areas within this limit as shown in Figures 2g–2l, so that the mean fluxes within these areas would be valid for calculating the escape rates. The results from the second method are shown in Table 1 as the numbers without parentheses and are better for both escape rate estimates and comparisons owing to more complete integration areas and less bias.

**Table 1.** Plume, Tail, and Total Ion Escape Rates for  $>6$  eV  $O^+$  Estimated at  $x = -1.6 R_M$  and  $z = 1.6 R_M$  as Shown in Figure 2<sup>a</sup>

		Time 1	Time 2	Time 1 and 2
Plume MSE- $z = 1.6 R_M$	Mean flux ( $10^6 \text{ cm}^{-2} \text{ s}^{-1}$ )	0.26	0.29	0.25
	Area ( $R_M^2$ )	17.2 (13.7)	17.2 (13.5)	17.2 (16.7)
	Escape rate ( $10^{24} \text{ s}^{-1}$ )	$0.52 \pm 0.04$ ( $0.41 \pm 0.03$ )	$0.57 \pm 0.06$ ( $0.44 \pm 0.04$ )	$0.50 \pm 0.05$ ( $0.47 \pm 0.04$ )
Tail MSE- $x = -1.6 R_M$	Mean flux ( $10^6 \text{ cm}^{-2} \text{ s}^{-1}$ )	1.3	0.84	0.95
	Area ( $R_M^2$ )	17.2 (12.6)	17.2 (13.7)	17.2 (16.2)
	Escape rate ( $10^{24} \text{ s}^{-1}$ )	$2.6 \pm 0.3$ ( $1.9 \pm 0.2$ )	$1.7 \pm 0.2$ ( $1.3 \pm 0.1$ )	$1.9 \pm 0.2$ ( $1.7 \pm 0.2$ )
Total escape plume + tail ( $10^{24} \text{ s}^{-1}$ )		$3.1 \pm 0.3$ ( $2.3 \pm 0.2$ )	$2.3 \pm 0.2$ ( $1.7 \pm 0.1$ )	$2.4 \pm 0.2$ ( $2.2 \pm 0.2$ )
Plume/total		17% (18%)	25% (26%)	21% (21%)

<sup>a</sup>The numbers with or without parentheses are calculated from the two different methods as described in section 3.

Table 1 summarizes the estimates of plume, tail, and total escape rates for  $>6$  eV  $O^+$  ions from the two time periods separately and together. The error bars for the escape rates are propagated from the standard deviations of the fluxes in Figures 2g–2l. Using the both methods described in the last paragraph to calculate escape rates, the variations between the two time periods are generally consistent: the tailward escape rate drops significantly ( $\sim 30\%$ ) from Time 1 to Time 2, while the plume escape rate does not change much ( $< 10\%$ ). It is worth noting that the data points in Figure 2h do not cover the area at  $x > \sim 2 R_M$ , where the fluxes are likely to be lower assuming the flux distribution is similar to Figure 2g. This is likely to be the main reason that the mean plume flux in Time 2 is higher than that in Time 1 and that including all data (see Table 1). The fact that including all data from the two time periods gives very close mean plume flux and escape rate to those in Time 1 also suggests that the plume flux distributions and escape rates do not vary significantly between the Time 1 and Time 2. The relative contribution from the plume escape increases from 17% to 25% when the total ion escape rate when the total ion escape rate for  $>6$  eV  $O^+$  drops from 3.1 to  $2.3 \times 10^{24} \text{ s}^{-1}$ .

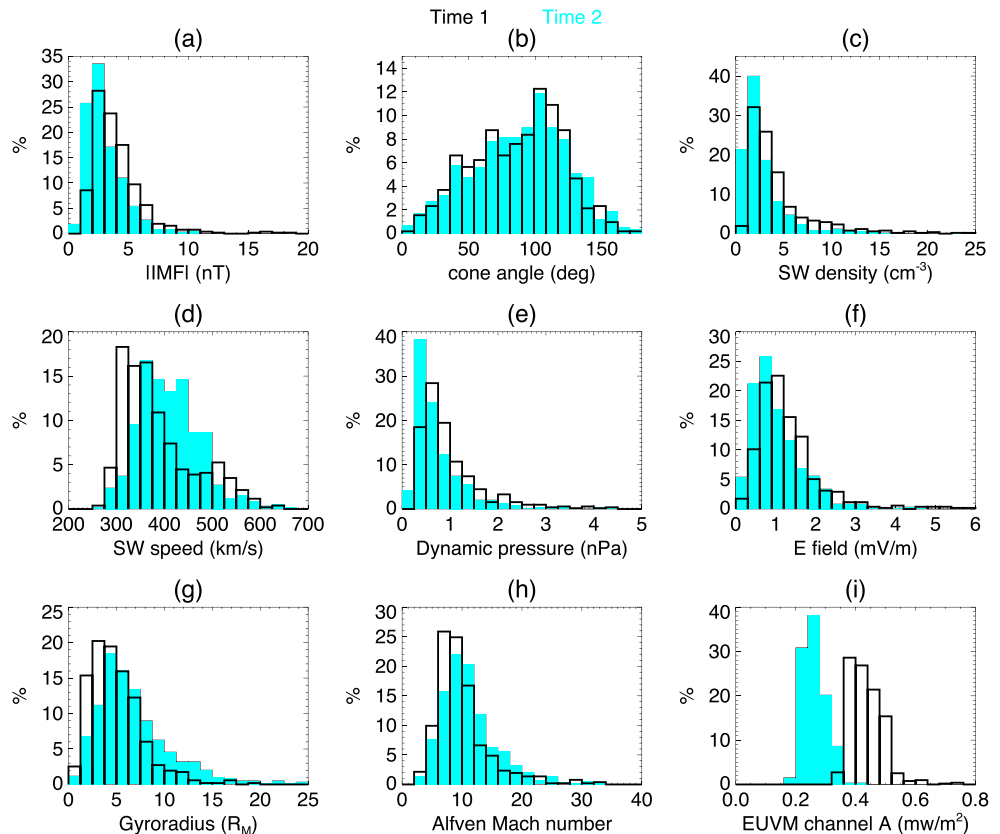


**Figure 3.** Histograms of orbital averaged upstream parameters.

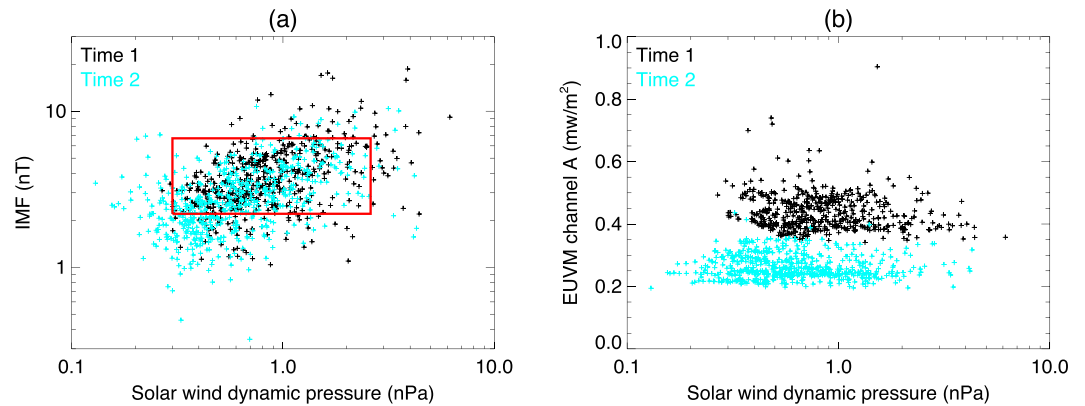


**Figure 4.** (a and b) Scatterplots of solar wind dynamic pressure versus IMF and EUV irradiances. The red box in Figure 4a labels the constrained solar wind (0.3–2.6 nPa) and IMF (2.2–6.7 nT) conditions.

### 4. Upstream Conditions

To understand the variations of ion escape between the two time periods, we have also performed a statistical study on the upstream conditions. Figure 3 shows the histograms of upstream parameters during the two time periods. The solar wind densities, speeds, and IMF vectors are measured by SWIA and MAG and averaged on an orbit-by-orbit basis [Halekas et al., 2016]. The EUV irradiances are also orbit-averaged data from Channel A of EUVM. The cone angle in Figure 3b is the angle between the IMF direction and the

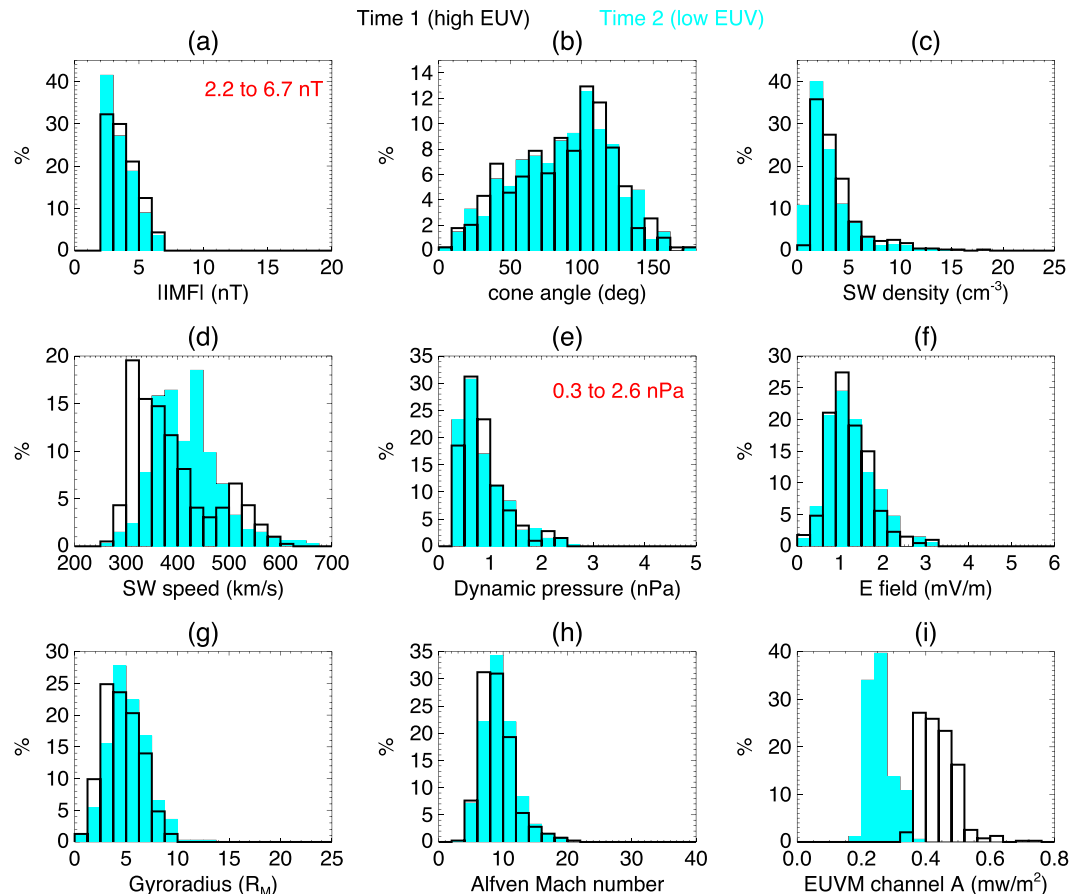


**Figure 5.** (a–i) Histograms of orbital averaged upstream parameters with constrained solar wind and IMF conditions, using only data within the red box in Figure 4a.

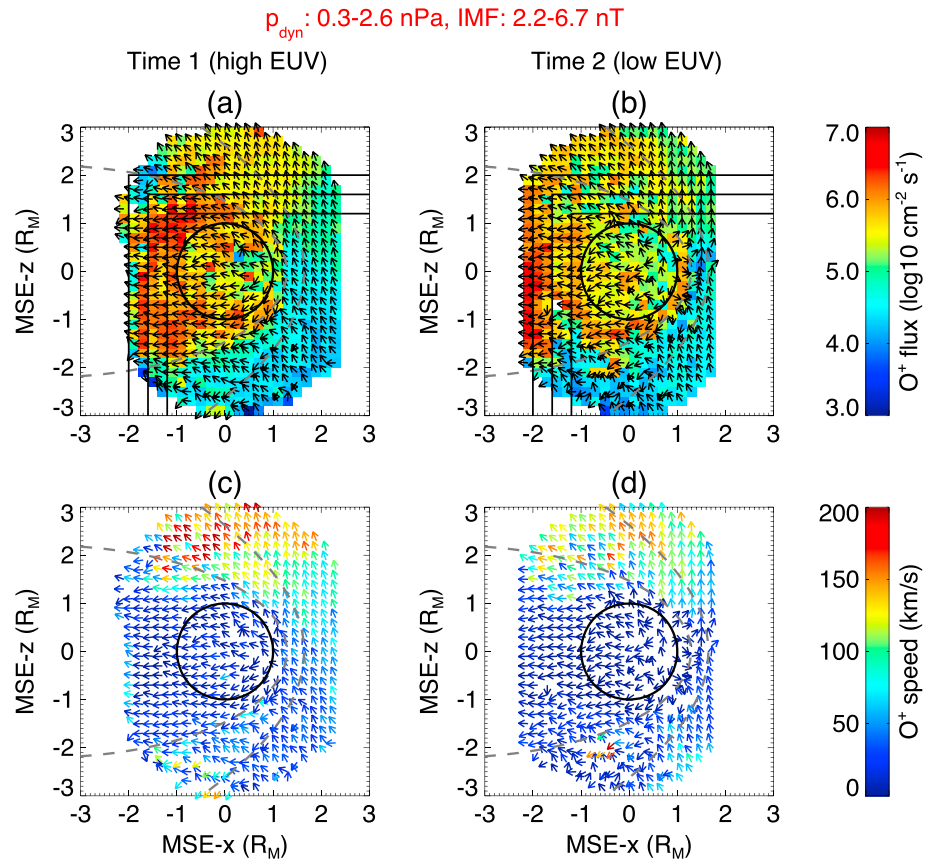


**Figure 6.**  $O^+$  flux and velocity maps during the two time periods with (a and c) high and (b and d) low EUV radiations, under the constrained solar wind and IMF conditions. The solid black lines in Figures 6a and 6b label the surfaces used to estimates the ion escape rates.

MSO/MSE  $x$  axis. Using the solar wind and IMF data, we also calculate the solar wind dynamic pressure  $p_{\text{dyn}} = m_p n_{\text{sw}} v_{\text{sw}}^2$ , upstream electric field  $\mathbf{E} = -\mathbf{v}_{\text{sw}} \times \mathbf{B}_{\text{IMF}}$ , pickup  $O^+$  gyroradius in the solar wind  $r_g = m_O v_{\text{sw}} \sin \theta_{\text{cone}} / (e B_{\text{IMF}})$ , and Alfvén Mach number  $M_A = v_{\text{sw}} / v_A$ , as these parameters can affect the plasma boundary locations ( $p_{\text{dyn}}$  and  $M_A$ ), ion acceleration ( $E$ ), and plume shape ( $r_g$ ). We can see that the solar EUV irradiance during Time 2 is significantly weaker than that during Time 1, with very little overlap (Figure 3i). It is because Mars moved farther away from the Sun from Time 1 to Time 2. There are differences in other parameter histograms between the two time periods as well, but not as distinct as that in the EUV histograms. The scatterplots in Figure 3 show that there are more data points from Time 2 with low IMF and solar wind  $p_{\text{dyn}}$  and that the IMF and  $p_{\text{dyn}}$  are correlated in general.

To investigate the solar EUV dependence of ion escape, we want to constrain the other solar wind and IMF parameters. Considering the limited data we have now, we put constraints on the solar wind  $p_{\text{dyn}}$  (0.3 to 2.6 nPa) and IMF strength (2.2 to 6.7 nT), as shown by the red box in Figure 4a. We have tried different numbers for these constraints, and the current combination gives the lowest statistical difference (in total chi-square) between the histograms of all solar wind and IMF related parameters as in Figures 3a–3h between the data sets from the two time periods.

Figure 5 shows the revised histograms of the upstream parameters after applying the constraints on IMF and  $p_{\text{dyn}}$  within the red box in Figure 4a. As shown in Figure 5i, the EUV histograms are still distinctly different with little overlap between Time 1 and Time 2. The histograms of the solar wind and IMF related parameter are close to each other between the two time periods, except for the solar wind speed (Figure 5d). This is not problematic because the more physically meaningful parameters, such as  $p_{\text{dyn}}$ ,  $E$ ,  $r_g$ , and  $M_A$ , have a similar probability distribution during the two time periods. Therefore, after the application of the data constraints the MAVEN ion measurements are under comparable upstream solar wind and IMF conditions but are

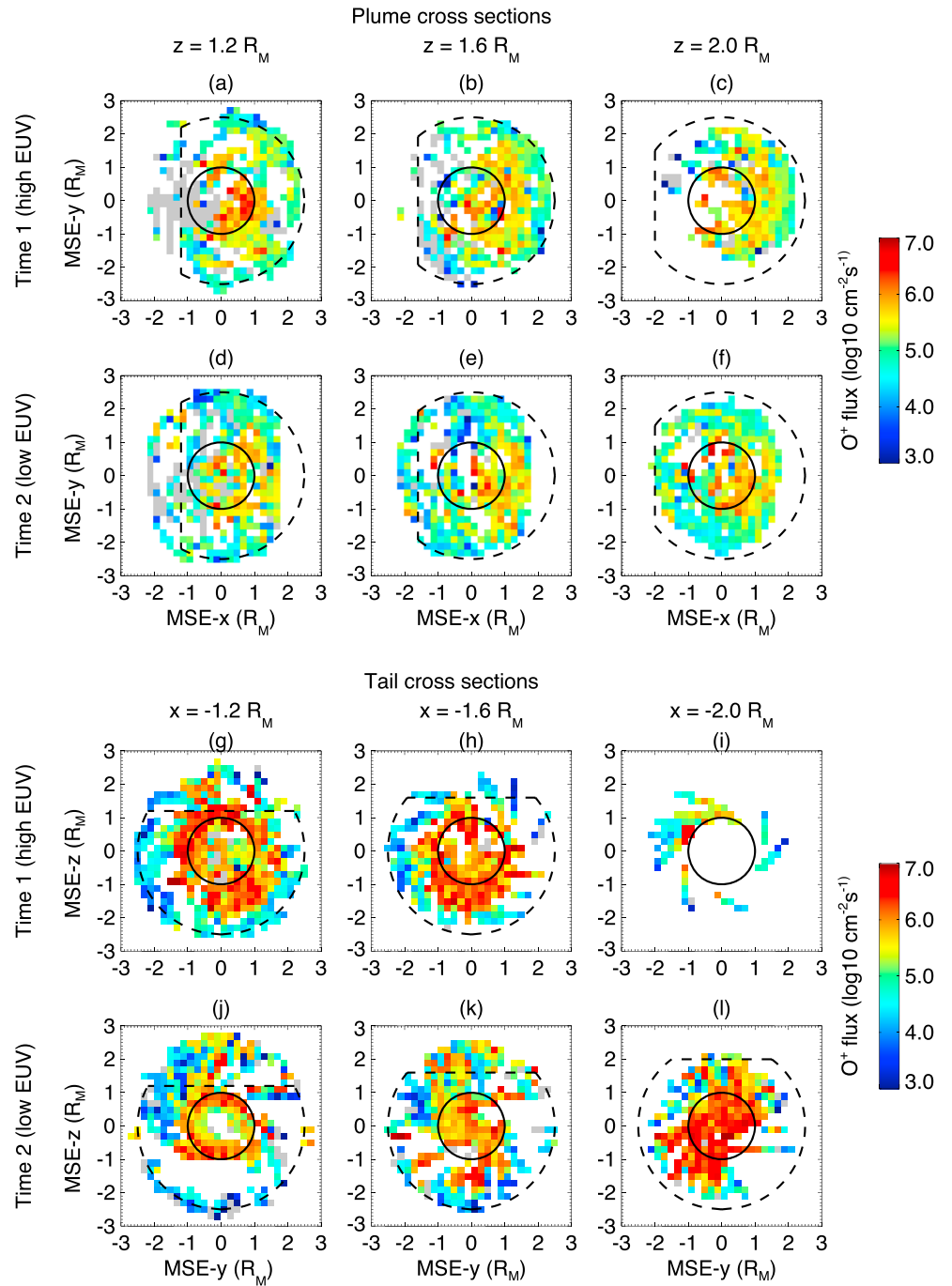


**Figure 7.** Escaping  $O^+$  ion fluxes through different (a–f) plume and (g–l) tail cross sections as labeled in Figure 6. The grey bins represent returning fluxes.

exposed to distinctly different solar EUV irradiances. The comparison of escaping ion flux distributions between the two time intervals enables us to distinguish the solar EUV effects.

## 5. Ion Escape Variations With Solar EUV Irradiance

### 5.1. Ion Flux and Velocity Distributions

Using the solar wind and IMF constraints as discussed in section 4, we perform the similar analysis as in section 3 to the  $>6\text{ eV } O^+$  data from Time 1 (high EUV) and Time 2 (low EUV). Figure 6 shows the

**Table 2.** Plume, Tail, and Total O<sup>+</sup> ion Escape Rates Estimated at Different Surfaces as Shown in Figures 6 and 7 During the Two Time Periods With High and Low EUV Fluxes under the Constrained Solar Wind and IMF Conditions (Section 4)<sup>a</sup>

	Time 1 (High EUV)			Time 2 (Low EUV)		
	$z = 1.2 R_M$	$z = 1.6 R_M$	$z = 2.0 R_M$	$z = 1.2 R_M$	$z = 1.6 R_M$	$z = 2.0 R_M$
Plume	Mean flux ( $10^6 \text{ cm}^{-2} \text{ s}^{-1}$ )	0.32	0.30	0.35	0.22	0.30
	Area ( $R_M^2$ )	15.6 (12.2)	17.2 (12.8)	18.6 (9.0)	15.6 (11.8)	17.2 (11.4)
	Escape rate ( $10^{24} \text{ s}^{-1}$ )	$0.57 \pm 0.08$ ( $0.42 \pm 0.06$ )	$0.59 \pm 0.05$ ( $0.43 \pm 0.03$ )	$0.74 \pm 0.05$ ( $0.36 \pm 0.02$ )	$0.39 \pm 0.08$ ( $0.28 \pm 0.05$ )	$0.60 \pm 0.05$ ( $0.39 \pm 0.03$ )
Tail	Mean flux ( $10^6 \text{ cm}^{-2} \text{ s}^{-1}$ )	$x = -1.2 R_M$ 1.1	$x = -1.6 R_M$ 1.2	$x = -2.0 R_M$ 0.44	$x = -1.2 R_M$ 0.68	$x = -1.6 R_M$ 0.75
	Area ( $R_M^2$ )	15.6 (13.6)	17.2 (10.8)	18.6 (3.2)	15.6 (9.8)	17.2 (10.8)
	Escape rate ( $10^{24} \text{ s}^{-1}$ )	$2.1 \pm 0.2$ ( $1.6 \pm 0.2$ )	$2.5 \pm 0.3$ ( $1.5 \pm 0.2$ )		$1.2 \pm 0.1$ ( $0.67 \pm 0.07$ )	$1.5 \pm 0.1$ ( $0.88 \pm 0.09$ )
Total escape: plume + tail ( $10^{24} \text{ s}^{-1}$ )	$2.7 \pm 0.2$ ( $2.0 \pm 0.2$ )	$3.1 \pm 0.3$ ( $1.9 \pm 0.2$ )		$1.6 \pm 0.1$ ( $0.95 \pm 0.09$ )	$2.1 \pm 0.1$ ( $1.3 \pm 0.1$ )	$4.1 \pm 0.3$ ( $2.4 \pm 0.2$ )
Plume/Total	21% (21%)	19% (23%)		24% (29%)	29% (30%)	18% (20%)

<sup>a</sup>The numbers with or without parentheses are calculated from the two different methods as described in section 3.

comparison of O<sup>+</sup> flux and velocity distributions between high and low EUV. Similar to the results in section 3, we see stronger tailward fluxes and higher plume velocities in Time 1 (high EUV) than those in Time 2 (low EUV).

The higher plume velocities in Time 1 indicate a more energetic plume under more intense solar EUV irradiance. Considering that the upstream electric field histograms are generally consistent between the two time periods as shown in Figure 5f, one possible explanation for a more energetic plume is a longer acceleration distance. A previous study of Martian plasma boundary location variations based on MEX data by *Edberg et al.* [2009] suggests that high EUV generally causes the magnetic pileup boundary (MPB) to move inward. As discussed in *Fang et al.* [2008], the plume ions are likely to be produced near or above the MPB so that they are accelerated by the strong electric field in the sheath region. In the case that the MPB is at lower altitude, more pickup ions created near the MPB will be accelerated over a longer distance to reach any certain position at high altitude in the +E hemisphere (i.e., the plume region) and will gain more energies.

## 5.2. Escape Rates

As shown in Figure 6, the stronger tailward fluxes in Time 1 indicate higher tailward escape rates under high the EUV condition. We estimate the escape rates through different surfaces: plume cross sections at  $z = 1.2$ ,  $1.6$ , and  $2.0 R_M$  and tail cross sections at  $x = -1.2$ ,  $-1.6$ , and  $-2.0 R_M$ , as shown by the solid black lines in Figures 6a and 6b. The ion fluxes through these surfaces are shown in Figure 7. We also use the two methods as described in section 3 to calculate the escape rates through these surfaces. The results are shown in Table 2. The escape rates in the parentheses are the results integrated over the data covered areas and serve as lower limit estimates. Those numbers without parentheses are obtained by calculating the mean fluxes and then extending to the integration areas as labeled by the dashed lines in Figure 7, which avoid the bias from different data covered areas and will be used for comparisons between the two time periods (high and low EUV). The error bars are propagated from the standard deviations of the fluxes shown in Figure 7. The escape rate at  $x = -2.0 R_M$  during Time 1 (high EUV) is not available due to the poor data coverage as shown in Figure 7i.

Figure 8a and Table 2 show that the total escape rate tends to increase moderately with the distance from the planet from ( $x = -1.2 R_M$ ,  $z = 1.2 R_M$ ) to ( $x = -1.6 R_M$ ,  $z = 1.6 R_M$ ). This is probably because at  $1.6 R_M$  more ions are accelerated to beyond the observation energy threshold (6 eV) and also more pickup ion sources at higher altitudes are included. However, there is an increase in both the tailward escape rate and the mean flux by more than a factor of 2 from  $x = -1.6$  to  $-2.0 R_M$  during Time 2 (low EUV) (see also Table 2). No comparison from Time 1 (high EUV) is available due to the poor data coverage at  $x = -2.0 R_M$ . In fact, the data coverage at  $x = -2.0 R_M$  during Time 2 (high EUV) is not good either. As shown in Figure 7l, the data only concentrate near the center of the tail, which may result in overestimates of the mean flux and escape rate. Thus, it is hard to tell whether this increase at  $x = -2.0 R_M$  is real or not. Overall, the escape rates estimated at  $1.2 R_M$  and  $1.6 R_M$  are reasonably consistent.

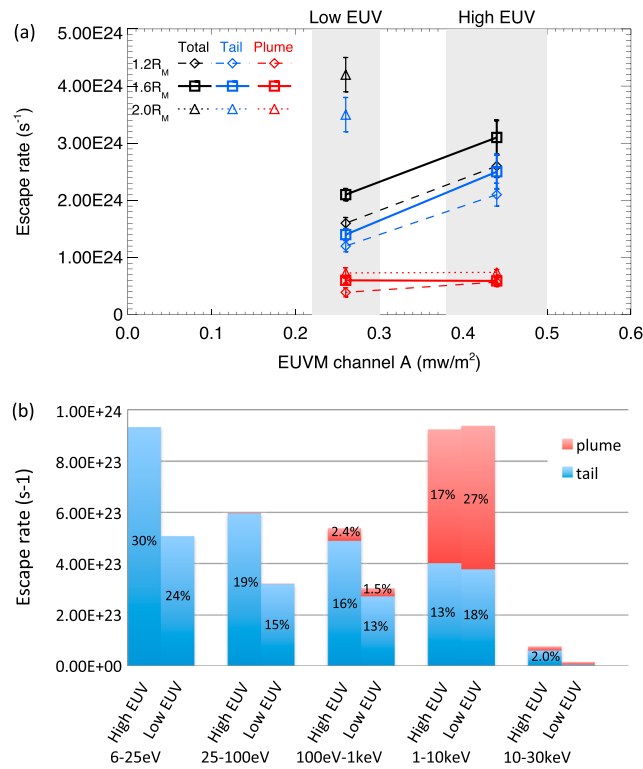


**Figure 8.** (a)  $>6\text{ eV O}^+$  escape rates estimated at different surfaces versus averaged EUV irradiances during the two time periods. The shaded areas show the standard deviations of the EUV irradiances. (b)  $\text{O}^+$  ion escape rates within different energy ranges estimated at  $x = -1.6 R_M$  and  $z = 1.6 R_M$ . The percentages (only labeled when  $>1\%$ ) show the ratio to the total  $\text{O}^+$  escape rate ( $6\text{ eV} - 30\text{ keV}$ ) under high or low EUV.

As shown in Figure 8a the tailward escape rates increase with EUV significantly, while the plume escape rates do not change much except for at  $z = 1.2 R_M$ . Since plume ions are likely to be generated near or above MPB and accelerated above MPB [Fang et al., 2008], it is better to estimate the plume escape rate through a surface at higher altitude. Thus, the plume escape rates at  $z = 1.6$  and  $2.0 R_M$  should be more accurate estimates, which do not show significant difference between low and high EUV conditions. The stronger EUV fluxes would generally enhance the ionization of neutral sources. However, it is possible that the enhancements of lower altitude sources, which mainly contribute to the tailward escape, are more significantly than those of the higher-altitude sources, which mainly contribute to the plume escape. Therefore, the increase of escape rate with EUV is mostly seen in the tail but not in the plume.

Estimating at the surfaces of  $x = -1.6 R_M$  and  $z = 1.6 R_M$ , where both the plume and tail cross sections have adequate data coverage during the two time periods as shown in Figure 7 and are at a reasonable distance from the planet, the total escape rate for  $>6\text{ eV O}^+$  increases from  $2.1$  to  $3.1 \times 10^{23}\text{ s}^{-1}$  with EUV irradiance from  $0.26$  to  $0.44\text{ mW/m}^2$ , by almost the same factor. In this work we used the data from Channel A of EUVM, which only covers a narrow wavelength band of  $17 - 22\text{ nm}$ . Under the same solar wind and IMF constrains, the averaged irradiances from the other two EUVM channels for Time 2 (low EUV) and Time 1 (high EUV) are  $0.22$  and  $0.52\text{ mW/m}^2$  from Channel B ( $0.1 - 7\text{ nm}$ , corresponding to soft X-ray) and  $2.8$  and  $4.3\text{ mW/m}^2$  from Channel C ( $121 - 122\text{ nm}$ , corresponding to Lyman  $\alpha$  line). Although it is not clear which channel can represent the variation of a complete EUV irradiance for  $\sim 10 - 120\text{ nm}$  better, comparing ion escape with irradiances from the three channels gives very similar results. Noticing that the seasonal variation of the solar EUV radiation between the two time periods that we investigated is small comparing to long-term EUV variations with solar cycle or over the history of the solar system, our results suggest that the ion escape rate may vary by a much larger factor with EUV over a longer time scale. Although the plume escape rate is not sensitive to the seasonal EUV variation, it may vary more significantly with long-term EUV variations.

### 5.3. Different Energy Ranges

To better understand the seasonal variation for different ion populations, we estimate the escape rates within different energy ranges at the surfaces of  $x = -1.6 R_M$  and  $z = 1.6 R_M$ , which have the best data coverage and a reasonable distance from the planet. The results are shown in Figure 8b.

As expected, the tailward escape is dominated by low-energy ions, while the plume ions are mainly between  $1$  and  $10\text{ keV}$  under both high and low EUV conditions. The tailward escape rate variations with EUV are mostly seen in the low-energy range at  $<1\text{ keV}$ . At  $>1\text{ keV}$ , both plume and tailward escape rates do not change much. As discussed in Dong et al. [2015], there is no clear boundary between the plume and tail regions, but a smooth transition region. Some of the high-energy ( $>1\text{ keV}$ ) tailward escaping ions are like

plume ions: generated near the MPB and accelerated in the sheath region but are deflected more by the magnetic field to the tail region depending on their initial positions and the electromagnetic field distribution [Fang *et al.*, 2010]. Meanwhile, the low-energy (<1 keV) tailward escaping ions are likely to be generated at lower altitude. Therefore, the fact that the ion escape rate increase is mostly from <1 keV ions can also be explained by a more significant enhancement of lower altitude sources under the high EUV conditions, as discussed in section 5.2.

The escape rate at >10 keV under high EUV is much larger than low EUV, although both numbers are very small comparing to other energy ranges. Under high EUV conditions, the >10 keV escape (mostly tailward) contributes ~2% to the total ion escape. For low EUV, the >10 keV escape rate is much lower and contributes <1% to the total escape. As discussed in our previous work [Dong *et al.*, 2015], there are upstream pickup  $O^+$  detected by STATIC at >10 keV with weak fluxes of  $\sim 10^4$ – $10^5$   $cm^{-2} s^{-1}$ . Comparing with the mean tailward fluxes  $\sim 10^6$   $cm^{-2} s^{-1}$  as shown in Table 2, it is plausible that the ~2% at >10 keV of the total ion escape during Time 1 (high EUV) is from upstream pickup ions that enter the tail region. This high-energy portion is more significant under high EUV, probably because the neutral corona and upstream  $O^+$  production are enhanced under high EUV. MAVEN observations of the hot O corona have shown positive correlation between the corona density and EUV flux based on the corona brightness at the altitudes of 700–1500 km (i.e.  $\sim 1.2$ – $1.5 R_M$ ) [Deighan *et al.*, 2015]. However, a more recent study by Rahmati *et al.* [2016] based on the upstream pickup ion data from MAVEN suggests that the more distant upstream hot O corona does not show significant seasonal variation. Thus, whether the seasonal O corona enhancement with EUV is enough to account for the >10 keV tailward escaping ions under high EUV condition requires more quantitative investigation.

## 6. Discussion

We have examined the ion escape during two time periods with and without the solar wind and IMF constraints. The ion flux and velocity distributions between Figures 2 and 6 (without and with the solar wind and IMF constraints, respectively) are generally consistent. The ion escape rates at  $1.6 R_M$  and the variations from Time 1 to Time 2 are also generally consistent between Tables 1 and 2. These imply that the most important factor in determining the difference in ion escape between the two time intervals is most likely the solar EUV intensity.

Our results show that the ion escape rate increases with EUV under the constrained solar wind dynamic pressure. This is generally consistent with the study of MEX data by Ramstad *et al.* [2015], which shows that the ion escape rate is higher under high EUV condition than that under low EUV with nominal solar wind speeds and densities. Lundin *et al.*'s [2008b] results suggest that the low-energy ion escape rate (30–800 eV) increases linearly with EUV, also generally consistent with our results within a similar energy range of 25 eV–1 keV. The work by Nilsson *et al.* [2010] did not find any clear correlation between the ion escape and solar EUV radiation. However, their work is based on a data set over a continuous time span with a single-peak solar EUV flux histogram. They divided the data set by the median EUV flux near the peak, so that most of the EUV fluxes from the two partial data sets are still close to the original median value. The EUV variation between the two data sets may not be enough for observable effects on ion escape. The two data sets we studied in this paper naturally have different EUV distributions because of the 3 month gap between the two time periods. Thus, the ion escape variation with EUV is significant enough to be observed. In addition, in Nilsson *et al.* [2010] the solar wind and IMF conditions are not controlled, which may also affect the ion escape variations.

In this work, we have extended the lower energy limit for data analysis from 25 eV as in our previous work with Time 1 data [Dong *et al.*, 2015] to 6 eV with spacecraft potential corrections. With updated data calibration and analysis, the tailward and plume escape rates at >25 eV during Time 1 from this work are still generally consistent with our previous results. However, the <6 eV ions escape can be a significant portion of the total ion loss. Further data calibrations will be required to include <6 eV ions. We have calculated the error bars for the escape rates through the propagation of the standard deviations of the mean fluxes in each bin of the ion flux maps. The instrument uncertainties are not included yet. For the solar EUV radiation, we have used the data from Channel A (17–22 nm) of EUVM. To better quantify the solar EUV dependence of ion escape and understand the mechanism, we will need to consider a full solar EUV

spectrum of ~10–124 nm and the ionization cross sections of neutral sources at different wavelengths. We seek to solve these issues in our future work with improved data calibrations and analysis methods.

The solar EUV variation can affect the neutral distribution, ion production, and plasma boundaries at Mars and consequently cause variations in ion escape. However, we cannot yet fully understand the mechanisms for some observed trends. Although we have constrained the solar wind and IMF conditions to determine the dependence on EUV, there can be seasonal variations from other parameters such as solar radiation at other wavelengths and crustal field locations [Edberg *et al.*, 2008; Fang *et al.*, 2017]. As shown in Figure 1, the orbital coverage is not exactly the same between the two periods. Dawn-dusk asymmetry [Dubinin *et al.*, 2008] may also cause variations in ion escape. These unanswered questions are beyond the scope of this study but will be interesting topics for future work.

## 7. Summary and Conclusions

We studied the  $>6\text{ eV O}^+$  data from MAVEN during two time intervals: one is between 11 November 2014 and 19 March 2015 (solar longitude (Ls) from 231.1 to 310.5) and the other is between 4 June 2015 and 24 October 2015 (Ls from 352.5 to 58.8). By imposing constraints on the solar wind dynamic pressure (0.3–2.6 nPa) and IMF (2.2–6.7 nT), we obtain similar probability distributions of the upstream solar wind and IMF parameters but distinctly different solar EUV conditions between the two time intervals. Therefore, by examining the systematic differences in escaping ion distributions and loss rates, we are able to assess the effects from the seasonal variation of solar EUV on ion loss at Mars. Our observations and conclusions are summarized below:

1. The total ion escape rate for  $>6\text{ eV O}^+$  under all solar wind, IMF, and EUV conditions is  $2.4 \times 10^{24}\text{ s}^{-1}$ .
2. The total ion escape rate increases from 2.1 to  $3.1 \times 10^{24}\text{ s}^{-1}$  as the EUV irradiance increase from 0.26 to  $0.44\text{ mW/m}^2$ , by almost the same factor. The increase is mostly from tailward escape.
3. The plume is more energetic under high EUV, but the plume escape rate does not vary significantly with the seasonal EUV change.
4. The plume contribution to the total ion escape is more important (~30%) under low EUV conditions than that (~20%) under high EUV condition.
5. The EUV is likely to be the most important upstream factor causing the variations in ion escape between the two time periods.

As discussed before, the solar EUV radiation can affect ion escape through many processes, although some mechanisms are not fully understood yet. Our study shows that the Martian ion escape rate is sensitive to the moderate seasonal EUV changes, which implies that there can be more drastic variations in the ion escape rate over a longer time scale with the EUV variations during solar cycle and over history of the solar system. Understanding the ion escape dependence on solar EUV radiation is important for the study of the long-term evolution of the Martian atmosphere.

### Acknowledgments

The MAVEN project is supported by NASA through the Mars Exploration Program. The authors thank Chris Fowler, Yuki Harada, Shaosui Xu, and Ed Thiemann for helpful discussions. The MAVEN data are available through the Planetary Data System.

### References

- Andersson, L., R. E. Ergun, G. T. Delory, A. Eriksson, J. Westfall, H. Reed, J. McCauly, D. Summers, and D. Meyers (2015), The Langmuir Probe and Waves (LPW) instrument for MAVEN, *Space Sci. Rev.*, *195*, 173–198, doi:10.1007/s11214-015-0194-3.
- Barabash, S., A. Fedorov, R. Lundin, and J.-A. Sauvaud (2007), Martian atmospheric erosion rates, *Science*, *315*(5811), 501–503, doi:10.1126/science.1134358.
- Brain, D. A., et al. (2015), The spatial distribution of planetary ion fluxes near Mars observed by MAVEN, *Geophys. Res. Lett.*, *42*, 9142–9148, doi:10.1002/2015GL065293.
- Brecht, S. H., and S. A. Ledvina (2006), The solar wind interaction with the Martian ionosphere/atmosphere, *Space Sci. Rev.*, *126*(1), 15–38, doi:10.1007/s11214-006-9084-z.
- Carlsson, E., et al. (2006), Mass composition of the escaping plasma at Mars, *Icarus*, *182*, 320–328, doi:10.1016/j.icarus.2005.09.020.
- Carlsson, E., D. Brain, J. Luhmann, S. Barabash, A. Grigoriev, H. Nilsson, and R. Lundin (2008), Influence of IMF draping direction and crustal magnetic field location on Martian ion beams, *Planet. Space Sci.*, *56*, 861–867, doi:10.1016/j.pss.2007.12.016.
- Cloutier, P. A., R. E. Daniell, and D. M. Butler (1974), Atmospheric ion wakes of Venus and Mars in the solar wind, *Planet. Space Sci.*, *22*(6), 967–990, doi:10.1016/0032-0633(74)90166-4.
- Connerney, J. E. P., J. Espley, P. Lawton, S. Murphy, J. Odom, R. Oliverson, and D. Sheppard (2015), The MAVEN magnetic field investigation, *Space Sci. Rev.*, doi:10.1007/s11214-015-0169-4.
- Curry, S. M., J. G. Luhmann, Y. Ma, M. W. Liemohn, C. Dong, and T. Hara (2015), Comparative pick-up ion distributions at Mars and Venus: Consequences for atmospheric deposition and escape, *Planet. Space Sci.*, doi:10.1016/j.pss.2015.03.026.
- Deighan, J., et al. (2015), MAVEN IUVS observation of the hot oxygen corona at Mars, *Geophys. Res. Lett.*, *42*, 9009–9014, doi:10.1002/2015GL065487.

- Dong, C., S. W. Bougher, Y. Ma, G. Toth, A. F. Nagy, and D. Najib (2014), Solar wind interaction with Mars upper atmosphere: Results from the one-way coupling between the multifluid MHD model and the MTGCM model, *Geophys. Res. Lett.*, *41*, 2708–2715, doi:10.1002/2014GL059515.
- Dong, Y., X. Fang, D. A. Brain, J. P. McFadden, J. S. Halekas, J. E. Connerney, S. M. Curry, Y. Harada, J. G. Luhmann, and B. M. Jakosky (2015), Strong plume fluxes at Mars observed by MAVEN: An important planetary ion escape channel, *Geophys. Res. Lett.*, *661*, 8942–8950, doi:10.1002/2015GL065346.
- Dubinin, E., et al. (2006), Electric fields within the Martian magnetosphere and ion extraction: ASPERA-3 observations, *Icarus*, *182*, 337–342, doi:10.1016/j.icarus.2005.05.022.
- Dubinin, E., G. Chanteur, M. Fraenz, R. Modolo, J. Woch, E. Roussos, S. Barabash, R. Lundin, and J. D. Winningham (2008), Asymmetry of plasma fluxes at Mars. ASPERA-3 observations and hybrid simulations, *Planet. Space Sci.*, *56*, doi:10.1016/j.pss.2007.12.006.
- Dubinin, E., M. Fraenz, A. Fedorov, R. Lundin, N. Edberg, F. Duru, and O. Vaisberg (2011), Ion energization and escape on Mars and Venus, *Space Sci. Rev.*, *162*, 173–211, doi:10.1007/s11214-011-9831-7.
- Edberg, N., M. Lester, S. Cowley, and A. Eriksson (2008), Statistical analysis of the location of the Martian magnetic pileup boundary and bow shock and the influence of crustal magnetic fields, *J. Geophys. Res.*, *113*, A08206, doi:10.1029/2008JA013096.
- Edberg, N. J. T., D. A. Brain, M. Lester, S. W. H. Cowley, R. Modolo, M. Fränz, and S. Barabash (2009), Plasma boundary variability at Mars as observed by Mars Global Surveyor and Mars Express, *Ann. Geophys.*, *27*, 3537–3550, doi:10.5194/angeo-27-3537-2009.
- Eparvier, F. G., P. C. Chamberlin, T. N. Woods, and E. M. B. Thiemann (2015), The solar extreme ultraviolet monitor for MAVEN, *Space Sci. Rev.*, *195*, 293–301, doi:10.1007/s11214-015-0195-2.
- Fang, X., M. W. Liemohn, A. F. Nagy, Y. Ma, D. L. De Zeeuw, J. U. Kozyra, and T. H. Zurbuchen (2008), Pickup oxygen ion velocity space and spatial distribution around Mars, *J. Geophys. Res.*, *113*, A02210, doi:10.1029/2007JA012736.
- Fang, X., M. W. Liemohn, A. F. Nagy, J. G. Luhmann, and Y. Ma (2010), Escape probability of Martian atmospheric ions: Controlling effects of the electromagnetic fields, *J. Geophys. Res.*, *115*, A04308, doi:10.1029/2009JA014929.
- Fang, X., et al. (2017), The Mars crustal magnetic field control of plasma boundary locations and atmospheric loss: MHD prediction and comparison with MAVEN, *J. Geophys. Res. Space Physics*, *122*, doi: 10.1002/2016JA023509, in press.
- Fränz, M., E. Dubinin, E. Nielsen, J. Woch, S. Barabash, R. Lundin, and A. Fedorov (2010), Transterminator ion flow in the Martian ionosphere, *Planet. Space Sci.*, *58*(1), 1442–1454, doi:10.1016/j.pss.2010.06.009.
- Halekas, J. S., E. R. Taylor, G. Dalton, G. Johnson, D. W. Curtis, J. P. McFadden, D. L. Mitchell, R. P. Lin, and B. M. Jakosky (2015), The solar wind ion analyzer for MAVEN, *Space Sci. Rev.*, *195*, 125–151, doi:10.1007/s11214-013-0029-z.
- Halekas, J. S., et al. (2016), Structure, dynamics, and seasonal variability of the Mars-solar wind interaction: MAVEN solar wind ion analyzer inflight performance and science results, *J. Geophys. Res. Space Physics*, *122*, 547–578, doi:10.1002/2016JA023167.
- Hara, T., K. Seki, Y. Futaana, M. Yamauchi, S. Barabash, A. O. Fedorov, M. Yagi, and D. C. Delcourt (2013), Statistical properties of planetary heavy-ion precipitations toward the Martian ionosphere obtained from Mars Express, *J. Geophys. Res. Space Physics*, *118*, 5348–5357, doi:10.1002/jgra.50494.
- Jakosky, B. M., et al. (2015), The Mars Atmosphere and Volatile Evolution (MAVEN) mission, *Space Sci. Rev.*, *21*, doi:10.1007/s11214-015-0139-x.
- Jarvinen, R., D. A. Brain, and J. G. Luhmann (2015), Planetary ion dynamics in the induced magnetospheres of Venus and Mars, *Planet. Space Sci.*, doi:10.1016/j.pss.2015.08.012.
- Kallio, E., H. Koskinen, S. Barabash, C. M. C. Nairn, and K. Schwingenschuh (1995), Oxygen outflow in the Martian magnetotail, *Geophys. Res. Lett.*, *22*, 2449–2452, doi:10.1029/95GL02474.
- Leblanc, F., et al. (2015), Mars heavy ion precipitating flux as measured by MAVEN, *Geophys. Res. Lett.*, *42*, 9135–9141, doi:10.1002/2015GL066170.
- Liemohn, M. W., B. C. Johnson, M. Fränz, and S. Barabash (2014), Mars Express observations of high altitude planetary ion beams and their relation to the “energetic plume” loss channel, *J. Geophys. Res. Space Physics*, *119*, 9702–9713, doi:10.1002/2014JA019994.
- Luhmann, J. G., and K. Schwingenschuh (1990), A model of the energetic ion environment of Mars, *J. Geophys. Res.*, *95*, 939–945, doi:10.1029/JA095iA02p00939.
- Lundin, R., A. Zakharov, R. Pellinen, H. Borg, B. Hultqvist, N. Pissarenko, E. M. Dubinin, S. W. Barabash, I. Liede, and H. Koskinen (1989), First measurements of the ionospheric plasma escape from Mars, *Nature*, *341*, 609–612, doi:10.1038/341609a0.
- Lundin, R., A. Zakharov, R. Pellinen, S. W. Barabash, H. Borg, E. M. Dubinin, B. Hultqvist, H. Koskinen, I. Liede, and N. Pissarenko (1990), ASPERA/Phobos measurements of the ion outflow from the Martian ionosphere, *Geophys. Res. Lett.*, *17*, 873–876, doi:10.1029/GL017i006p00873.
- Lundin, R., et al. (2004), Solar wind-induced atmospheric erosion at Mars: First results from ASPERA-3 on Mars express, *Science*, *305*, 1933, doi:10.1126/science.1101860.
- Lundin, R., S. Barabash, M. Holmström, H. Nilsson, M. Yamauchi, M. Fraenz, and E. M. Dubini (2008a), A comet-like escape of ionospheric plasma from Mars, *Geophys. Res. Lett.*, *35*, L18203, doi:10.1029/2008GL034811.
- Lundin, R., S. Barabash, A. Fedorov, M. Holmstrom, H. Nilsson, J.-A. Sauvaud, and M. Yamauchi (2008b), Solar forcing and planetary ion escape from Mars, *Geophys. Res. Lett.*, *35*, L09203, doi:10.1029/2007GL032884.
- Lundin, R., S. Barabash, M. Holmstrom, H. Nilsson, Y. Futaana, R. Ramstad, M. Yamauchi, E. Dubinin, and M. Fraenz (2013), Solar cycle effects on the ion escape from Mars, *Geophys. Res. Lett.*, *40*, 6028–6032, doi:10.1002/2013GL058154.
- McFadden, J. P., et al. (2015), The MAVEN Suprathermal and Thermal Ion Composition (STATIC) Instrument, *Space Sci. Rev.*, doi:10.1007/s11214-015-0175-6.
- Mitchell, D. L., et al. (2016), The MAVEN solar wind electron analyzer, *Space Sci. Rev.*, *200*, 495, doi:10.1007/s11214-015-0232-1.
- Najib, D., A. F. Nagy, G. Tóth, and Y. Ma (2011), Three-dimensional, multifluid, high spatial resolution MHD model studies of the solar wind interaction with Mars, *J. Geophys. Res.*, *116*, A05204, doi:10.1029/2010JA016272.
- Nilsson, H., E. Carlsson, D. A. Brain, M. Yamauchi, M. Holmström, S. Barabash, R. Lundin, and Y. Futaana (2010), Ion escape from Mars as a function of solar wind conditions: A statistical study, *Icarus*, doi:10.1016/j.icarus.2009.03.006.
- Nilsson, H., N. Edberg, G. Stenberg, and S. Barabash (2011), Heavy ion escape from Mars, influence from solar wind conditions and crustal magnetic fields, *Icarus*, doi:10.1016/j.icarus.2011.08.003.
- Rahmati, A., et al. (2016), MAVEN measured oxygen and hydrogen pickup ions: Probing the Martian exosphere and neutral escape, *J. Geophys. Res. Space Physics*, *122*, doi:10.1002/2016JA023371.
- Ramstad, R., Y. Futaana, S. Barabash, H. Nilsson, S. M. del Campo B, R. Lundin, and K. Schwingenschuh (2013), Phobos 2/ASPERA data revisited: Planetary ion escape rate from Mars near the 1989 solar maximum, *Geophys. Res. Lett.*, *40*, 477–481, doi:10.1002/grl.50149.

- Ramstad, R., S. Barabash, Y. Futaana, H. Nilsson, X. D. Wang, and M. Holmström (2015), The Martian atmospheric ion escape rate dependence on solar wind and solar EUV conditions: I. Seven years of Mars Express observations, *J. Geophys. Res. Planets*, *120*, 1298–1309, doi:10.1002/2015JE004816.
- Vignes, D., C. Mazelle, H. Rme, M. H. Acuña, J. E. P. Connerney, R. P. Lin, D. L. Mitchell, P. Cloutier, D. H. Crider, and N. F. Ness (2000), The solar wind interaction with Mars: Locations and shapes of the bow shock and the magnetic pile-up boundary from the observations of the MAG/ER Experiment onboard Mars Global Surveyor, *Geophys. Res. Lett.*, *27*, 49–52, doi:10.1029/1999GL010703.